Advances in Civil Engineering

RESEARCH ARTICLE OPEN ACCESS

Study on Vibration Superposition Induced by Dual-Line Subway Train Operation in Submerged Tunneling Sections

Yunsi Liu | Yueyuan Huang | Yuxiao Wu

School of Civil Engineering, Hunan University of Science and Technology, Xiangtan 411201, China

Correspondence: Yunsi Liu (liuyunsi@hnust.edu.cn)

Received: 14 January 2026 | **Revised:** 26 May 2026 | **Accepted:** 2 June 2026

Academic Editor: Shikha Binwal

Keywords: coupled simulation | dual-track line | newly constructed tunnel section | vibration response | vibration superposition | VMD

ABSTRACT

Accurately predicting the vibration response when a new tunnel passes beneath an existing double-track railway represents a major challenge in assessing the environmental impact of urban underground engineering. Traditional numerical simulations rely heavily on noisy field-measured signals and simplified single-source assumptions, leading to significant errors in complex multisource scenarios. To achieve refined vibration response simulation, this paper proposes a FLAC3D simulation method integrating Variational Mode Decomposition (VMD) signal denoising with multisource vibration superposition theory. The VMD algorithm (with optimized parameters $K = 8$, $\alpha = 2500$) is applied to denoise field-measured vibration signals, achieving a correlation coefficient of 0.9861 between the denoised and original signals—a 23.7% improvement over conventional denoising methods. Subsequently, based on vibration superposition theory, a multisource input model accounting for propagation path attenuation is constructed. Finally, high-precision dynamic calculations are performed within FLAC3D. The reliability of the proposed method is validated by comparing results with field measurements, showing a reduction in peak acceleration prediction error from 18.6% (using un-denoised signals) to 6.8% (using the proposed method). The study analyzes the combined effects of source magnitude, source location, and propagation attenuation. Results indicate that the superposition generated by double-track operation is not a simple numerical summation; the measured superposition value at the center point C2 is 1.54 times the average of the two individual responses, indicating constructive interference. The strongest vibration superposition effect occurs at C2, with a limited influence range—only the tunnel crown experiences significant vibration superposition (superposition rate of 54.6% at roof monitoring point P1, decreasing to less than 10% at the invert). This research provides new computational tools and methods for vibration studies in underground transportation networks.

1 | Introduction

In recent years, with the continuous expansion of China's rail transit network, newly constructed subway tunnels inevitably require passing beneath existing double-track lines. The long-term cyclic loads generated by the operation of existing double-track trains are transmitted to the tunnel sections passing underneath [1, 2], leading to a reduction in the strength of the initial support and posing a threat to structural safety (Table 1). Research on vibration response under such complex conditions remains in its developmental stage, with the primary challenge lying in accurately modeling the vibration superposition system under dual-track train loads. Therefore, conducting in-depth studies on the vibration response of newly constructed tunnel sections crossing beneath existing dual-track lines not only aids

This is an open access article under the terms of the Creative Commons Attribution License, which permits use, distribution and reproduction in any medium, provided the original work is properly cited.

Copyright © 2026 Yunsi Liu et al. *Advances in Civil Engineering* published by John Wiley & Sons Ltd.

TABLE 1 | Adverse effects caused by subway train vibration.

Number	Location	Spatial relationships	Problem	Literature
1	Tehran Metro	Parallel adjacency	Vibration superposition	[3]
2	Chongqing Metro	Parallel adjacency	Vibration superposition	[4]
3	Nanjing Metro Line 3	Parallel adjacent	Vibration superposition	[5]
4	Beijing Metro	Parallel adjacency	Vibration superposition	[6]
5	Beijing Intercity	Vertical underpass	Vibration superposition	[7]
6	Wuhan Metro Line 7	Parallel adjacent	Vibration superposition	[8]
7	Tianjin Metro Line 6	Vertical underpass	Ground subsidence	[9]
8	Hangzhou Metro	Parallel adjacent	Vertical cracks	[10]
9	Beijing Metro	Parallel adjacency	Foundation settlement	[11]
10	Baiyun Railway Station	Parallel adjacency	Vibration amplification	[12]
11	Shuangliu Airport Station	Overlapping underpass	Vibration amplification	[13]
12	Beijing-Shanghai High-Speed Railway	Parallel adjacency	Vibration amplification	[14]

in predicting vibration responses for crossing projects but also provides technical support for ensuring operational safety.

The measured vibration signals are heavily contaminated with noise, and direct analysis of raw data can easily introduce bias. To mitigate noise in the measurements, Oral et al. [15] proposed a transient vibration and noise reducer designed to minimize the peak vibrations and noise generated during the transient start-up and shutdown phases of machines with harmonic motion. Xie et al. [16] developed a novel deep residual U-Net-based denoising method to mitigate noise in vertical vibration signals of elevator cabins. To address the problem that measured responses inevitably suffer from noise contamination, which prevents accurate modal parameter estimation, Bao et al. [17] developed an operational modal analysis (OMA) program named NExT-SLRA-CE. This program removes noise from the measured environmental vibration responses. Its effectiveness was validated through numerical simulations of a four-story shear wall building subjected to white noise excitation. Tao et al. [18] identified substantial noise in collected vibration signals that interferes with feature analysis and leakage identification. They proposed the Adaptive Sparrow Search Algorithm–Variational Mode Decomposition–Self-Information (ASSA–VMD–SI) and Frechet pipeline vibration methods for noise reduction. Dalmasso et al. [19] proposed a Conditional Generative Adversarial Network (CGAN) technique as a strategy for constructing hybrid datasets, thereby increasing the available monitoring data for tunnels and overcoming the problem of data scarcity. Similarly, Dalmasso et al. [20] conducted a direct comparison of the dynamic responses of shallow submerged tunnels constructed in soft soil using the immersed tube method and deep tunnels excavated in sandstone and shale, thereby addressing the limitations in data recording and quantitative measurement for different types of tunnels. Qi et al. [21] addressed the complexity of manually selecting the decomposition layer number K in traditional VMD algorithms. They proposed an optimized VMD algorithm with adaptive K-selection. Applying this optimized VMD to noisy signals demonstrated improved reconstruction of absorbed signals and enhanced measurement accuracy compared to conventional denoising methods.

For the numerical simulation of train vibration response, Zheng et al. [22] employed the finite difference software FLAC3D to conduct dynamic analysis, validating the reliability of the numerical model through on-site train vibration tests. Mahmoudi and Rajabi [23] employed the finite difference software FLAC 3D to model tunnels adjacent to karst cavities, investigating how the location, size, distance, shape, and arrangement of these cavities affect displacement, bending moment, and axial force in tunnel linings. Gu et al. [24] employed the FLAC3D finite difference method to investigate the dynamic response of surrounding soil layers induced by train vibrations, applying artificially determined excitation force functions to the tunnel model. Xiao et al. [25] proposed a novel GZZ-based constitutive model and implemented it within FLAC3D, significantly enhancing the computational efficiency. Consequently, incorporating sound computational theories into FLAC3D contributes to improved calculation accuracy.

Although previous studies have addressed signal noise reduction, numerical simulation of train vibrations, or vibration superposition effects separately, several challenges remain. Existing noise reduction methods often rely on manually selected decomposition parameters, limiting their adaptability. Multisource vibration superposition models rarely account for propagation path attenuation in a physically consistent manner, and there is no integrated framework linking high-precision signal processing with three-dimensional numerical simulation of multisource scenarios. To address these issues, this paper establishes a VMD-based vibration signal denoising workflow, construts a multisource superposition vibration model in FLAC3D, integrates the denoised signal with the multisource superposition model, and completes dynamic calculations within FLAC3D. This forms a complete technical chain from signal processing to theoretical modeling and numerical simulation. By comparing simulation results under different operating conditions, the proposed coupling method is demonstrated to more accurately reflect actual

vibration responses, providing a more precise analytical tool for vibration prediction and control in similar underpass projects.

2 | Case Study

As shown in Figure 1a, the new Line 17 tunnel passes beneath the existing Lines 10 and 14. The Shilihe station serves as a three-line interchange station, forming a "T"-shaped transfer with the existing Shilihe stations of Lines 10 and 14. The new tunnel has a burial depth of approximately 22.904 m and a total length of 132.2 m. The minimum clearance between the tunnel structure and the base slab of the existing station's main structure is approximately 2.25 m. The tunnel has a horseshoe-shaped cross-section with excavation dimensions of 8.65 m × 9.92 m, a primary support thickness of 350 mm, and a secondary lining thickness of 350 mm. The tunnel section was constructed using the mining method. Line 10 and Line 14 were already in operation before tunnel construction began on Line 17. As shown in Figure 1b, during the construction of Line 17, support work was carried out, and shotcrete was applied to the tunnel structure. However, concrete fragments fell from the roof section as trains passed on the existing lines, posing a safety hazard to the construction work.

3 | Noise Reduction Processing of Measured Vibration Signals Based on VMD

3.1 | VMD Algorithm Principles and Parameter Optimization

The VMD algorithm is robust against sampling and noise, and can maintain constant noise reduction metrics even when its parameters are varied. At the same time, it can effectively avoid the phenomenon of modal aliasing. In the VMD algorithm [26, 27], the eigenmodal function is redefined as an amplitude-frequency modulated signal as follows:

$$u_k(t) = A_k(t)\cos\left(2\pi\int_0^t f_k(t)\mathrm{d}t + \phi_k(t)\right), \tag{1}$$

where $A_k(t)$ and $\varphi_k(t)$ are envelopes and phases, $f_k(t)$ is the instantaneous frequency, and $\mathrm{d}\varphi_k(t)/\mathrm{d}t \geq 0$; the envelope is non-negative, $A_k(t) \geq 0$; and $A_k(t)$ and the instantaneous frequency $f_k(t) = (1/2\pi)\cdot\mathrm{d}\varphi_k(t)/\mathrm{d}t$ are slowly varying for the phase $\varphi_k(t)$.

The VMD problem consists of finding a set of modes u_k that can reconstruct the given input signal $f(t)$ in a least-squares sense, while each mode is constrained to be mostly compact around a central frequency ωk estimated online as follows:

$$\min_{\{u_k\}\{\omega_k\}}\left\{\sum\left\{\partial_t\left[\left(\delta(t)+\frac{j}{\pi t}\right)\times u_k(t)\right]e^{-j\omega_k t}\right\}_2^2\right\}, \tag{2}$$

$$s.t.\sum_{k=1}^{K} u_k = f(t), \tag{3}$$

where u_k is the k modal components obtained by decomposition, ω_k is the frequency center of each component, and $\delta(t)$ is the pulse function.

To solve the constrained reconstruction problem, the quadratic penalty term and the Lagrange multiplier λ are invoked. Usually, in the presence of noise, Gaussian noise, the quadratic penalty is the classical method for reconstruction fidelity. The Lagrange multiplier is a common method to strictly enforce the constraint. Therefore, the augmented Lagrangian matrix is introduced as follows:

$$L(\{u_k\},\{\omega_k\},\lambda) = \alpha\sum_k\left\|\partial_t\left[\left(\delta(t)+\frac{j}{\pi}\right)\times u_k(t)\right]e^{-j\omega_k t}\right\|_2^2. \tag{4}$$

The VMD algorithm decomposes the signal into k eigenmodal functions by iteration, and the expression of u_k, ω_k, and λ after alternate merit-seeking iterations is as follows:

$$\hat{u}_k^{n+1}(\omega) = \frac{\hat{f}(\omega) - \sum_{i<k}\hat{u}_i^{n+1}(\omega) - \sum_{i>k}\hat{u}_i^{n}(\omega) + \frac{\hat{\lambda}^n(\omega)}{2}}{1+2\alpha(\omega-\omega_k^n)^2}, \tag{5}$$

$$\omega_k^{n+1} = \frac{\int_0^\infty \omega|\hat{u}_k^{n+1}(\omega)|^2 d\omega}{\int_0^\infty |\hat{u}_k^{n+1}(\omega)|^2 d\omega}, \tag{6}$$

$$\hat{\lambda}^{n+1}(\omega) = \hat{\lambda}^n(\omega) + \tau\left(\hat{f}(\omega) - 7\sum_k \hat{u}_k^{n+1}(\omega)\right), \tag{7}$$

where ω is frequency, τ is noise tolerance, and the Fourier transform of $f(t), \hat{u}_k^{n+1}(t)$ is $\hat{f}(\omega), \hat{u}_k^{n+1}(\omega), \hat{u}_i(\omega), \hat{\lambda}^n(\omega)$.

When the convergence condition is satisfied, the iteration is completed, and the final result is output as follows:

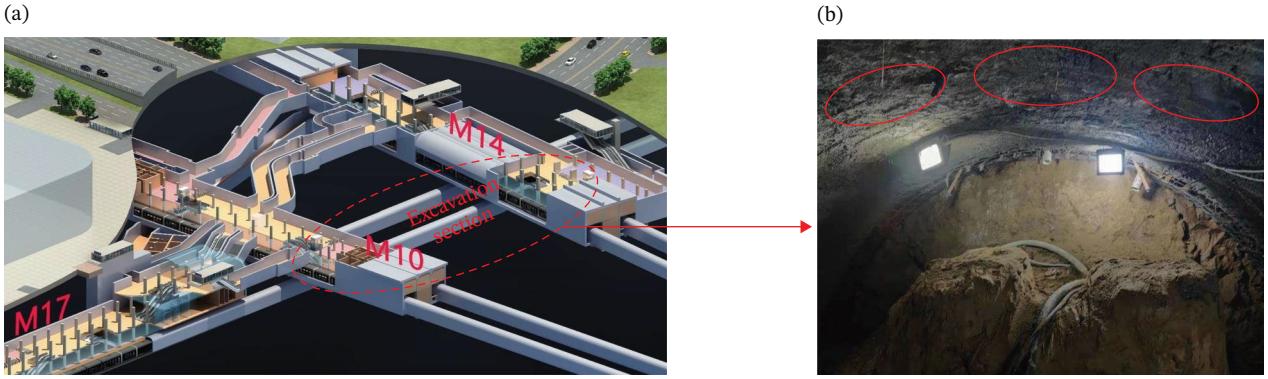


FIGURE 1 | Project overview diagram. (a) Underground tunnel section passing beneath existing double-track railway and (b) location of concrete spalling.

$$\frac{\sum_k ||\widehat{u}_k^{n+1} - \widehat{u}_k^n||_2^2}{||\widehat{u}_k^n||_2^2} < \varepsilon, \tag{8}$$

where ε is the convergence tolerance, set to 1×10^{-6}.

The value of k must be set according to the specific signal characteristics. An excessively small k-value may result in under-decomposition, preventing the complete extraction of effective components. Conversely, an excessively large k-value may lead to over-decomposition, yielding unnecessary spurious components that compromise the evaluation of the final solution. The selection of k must balance the avoidance of modal overlap with the preservation of signal characteristics, ensuring that the intrinsic mode function (IMF) componets obtained after VMD decomposition retain all feature information from the original signal.

The model noise reduction results are required to approximate the original vibration signal (the smaller the algorithm approximation degree mean squared error $(\mathrm{MSE})_f$, the better, and for comparison with subsequent indicators, the closer the algorithm approximation degree MSE_f^{-1} is to 1, the better), and the noise reduction signal results are also required to be sufficiently similar to the original vibration signal (the closer the algorithm correlation degree $|\rho_f|$ is to 1, the better). Therefore, the criteria for determining a good noise reduction algorithm are established as follows:

Binding conditions were as follows:

$$\max\left\{\mathrm{MSE}_f^{-1}\right\}, \tag{9}$$

$$\max\left\{\left|\rho_f\right|\right\}, \tag{10}$$

Where y_i is signal after noise reduction, y_i' is original signal; $\mathrm{MSE} = \sqrt{\frac{\sum_n (y_i - y_i')}{n}}$, $|\rho_f| = |\frac{\mathrm{cov}(y_i, y_i')}{\sqrt{D(y_i)}\sqrt{D(y_i')}}|$, $\mathrm{cov}(y_i, y_i')$ is the covariance of y_i, and y_i'; $\sqrt{D_y}$ is standard deviation.

Noise reduction algorithm f objective function is given as follows:

$$\max\{f\} = \max\left\{\gamma \mathrm{MSE}_f^{-1} + (1-\gamma)\left|\rho_f\right|\right\}, \tag{11}$$

where γ is the algorithm approximation impact factor, $1-\gamma$ is the correlation impact factor; in this paper, γ takes the value of 0.3.

3.2 | On-Site Monitoring

On-site monitoring utilizes the L20-S (vibration recorder frequency range: 0.1–1000 Hz) with a level-triggered mode, a trigger level of 0.001 g, and a storage duration of up to 20 s, as shown in Figure 2. When installing the sensors, a rigid bond was ensured with the tunnel so that the sensor and the tunnel form a single unit. At the same time, the correct installation orientation of the sensors was ensured to clearly identify the measurement values in all directions at the measurement point:

1. For roof monitoring, the X-axis is oriented along the tunnel advance direction, the Y-axis is perpendicular to the sidewall, and the Z-axis is perpendicular to the floor.
2. For sidewall monitoring, the X-axis is oriented along the tunnel advance direction, the Y-axis is perpendicular to the floor, and the Z-axis is perpendicular to the sidewall.
3. For floor monitoring, the X-axis is oriented along the tunnel advance direction, the Y-axis is perpendicular to the sidewall, and the Z-axis is perpendicular to the floor.

Representative signals were selected by averaging the three measurements with the highest signal-to-noise ratio, excluding measurements affected by non-train-related disturbances.

The monitoring layout for the existing lines is shown in Figure 3. 10-1, 10-2, and 10-3 denote the corresponding monitoring positions on the existing Line 10; 14-1, 14-2, and 14-3 denote the



FIGURE 2 | Monitoring equipment. (a) L20-S vibration recorder and (b) sensor.

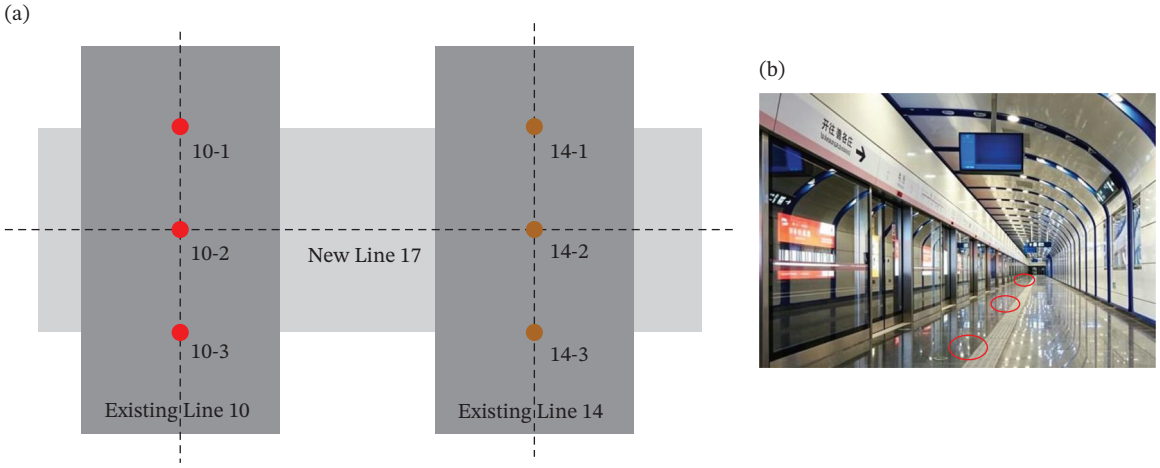


FIGURE 3 | Existing line monitoring points. (a) Monitoring point layout plan and (b) field monitoring site.

corresponding monitoring positions on the existing Line 14. The new tunnel features a double-pilot tunnel design, consisting of an upper pilot tunnel and a lower pilot tunnel. These auxiliary structures are constructed ahead of the main tunnel excavation to facilitate ground stabilization and provide access for monitoring. The monitoring point layout for the new tunnel is shown in Figure 4. Monitoring points were arranged along the tunnel excavation direction. Four monitoring sections (a1–a4) are established for the underpass beneath Line 10, with each monitoring point spaced 6.0 m apart. Seven monitoring sections (b1–b7) were established during the underpass of Line 14, with each monitoring point spaced 4.0 m apart. One point is taken from the bottom, top, and each side wall, with monitoring conducted in both the upper and lower pilot tunnels of the underpass section (p1–p8).

3.3 | Signal Noise Reduction

3.3.1 | Original Signal Noise Reduction

Figure 5 shows the vibration signal at monitoring section a2. The vibration signal at point p1 was selected for noise reduction. The sampling frequency was set to 1000 Hz with a duration of 20 s, and the number of sampling points was 2000.

When performing signal decomposition using the VMD algorithm, the convergence tolerance (tol) was set to 1×10^{-6}. The penalty factor α is determined through trial calculations with values of 5500, 5000, 4500, 4000, 3500, 3000, and 2500, and the corresponding correlation coefficient $|\rho_f|$ is evaluated. As shown in Figure 6, the correlation coefficient $|\rho_f|$ was evaluated for k-values ranging from 2 to 9. As α decreases, the filtering bandwidth of each mode narrows, raising the risk of mode mixing if α is too small. At $\alpha=2500$, the correlation coefficient reaches a maximum of 0.9861. When α is increased to 3000, the maximum correlation drops to 0.973 due to over-smoothing, and the trend becomes more pronounced for larger α. Conversely, preliminary tests with $\alpha<2500$ (not included in Figure 6 for clarity) yielded visible modal aliasing and a marked decline in correlation. Therefore, $\alpha=2500$ is selected as the optimal penalty factor that best balances noise reduction and signal fidelity.

For the number of variational modes, K, the center frequency method was employed. Under the condition of $\alpha=2500$, the center frequencies of the IMFs corresponding to different values of K were determined and are shown in Table 2. When $K=9$, the center frequency of IMF1 suddenly changed to 3.01 Hz, indicating an over-decomposition; when $K=5$, 6, 7, and 8, the main frequencies of each IMF component remained relatively stable. Combining this with the correlation metrics in Figure 6, K is ultimately set to 8.

The resulting IMF components obtained from the VMD decomposition of the original signal are shown in Figure 7. A total of eight IMF components and one noise component were obtained.

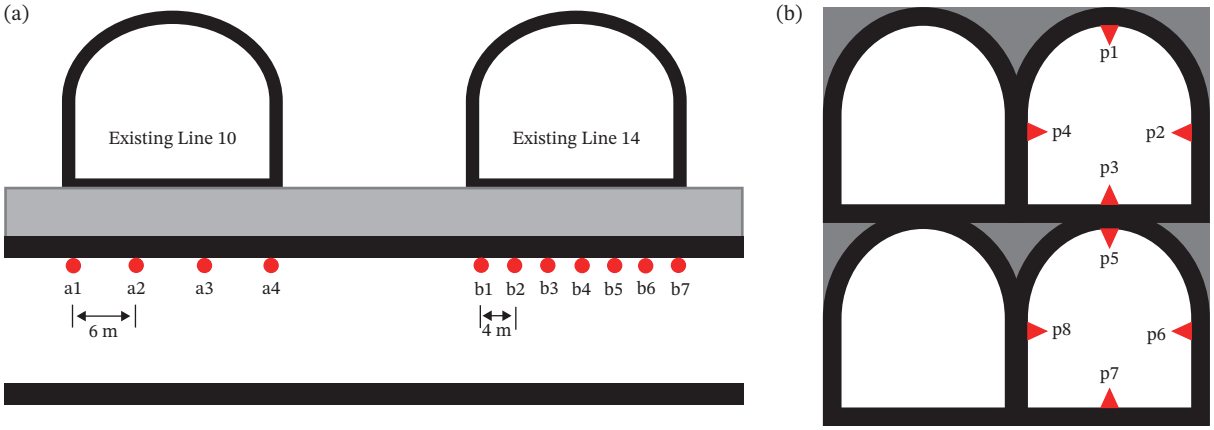


FIGURE 4 | Arrangement of monitoring points for new tunnel intervals. (a) Excavation direction layout and (b) excavation face layout.

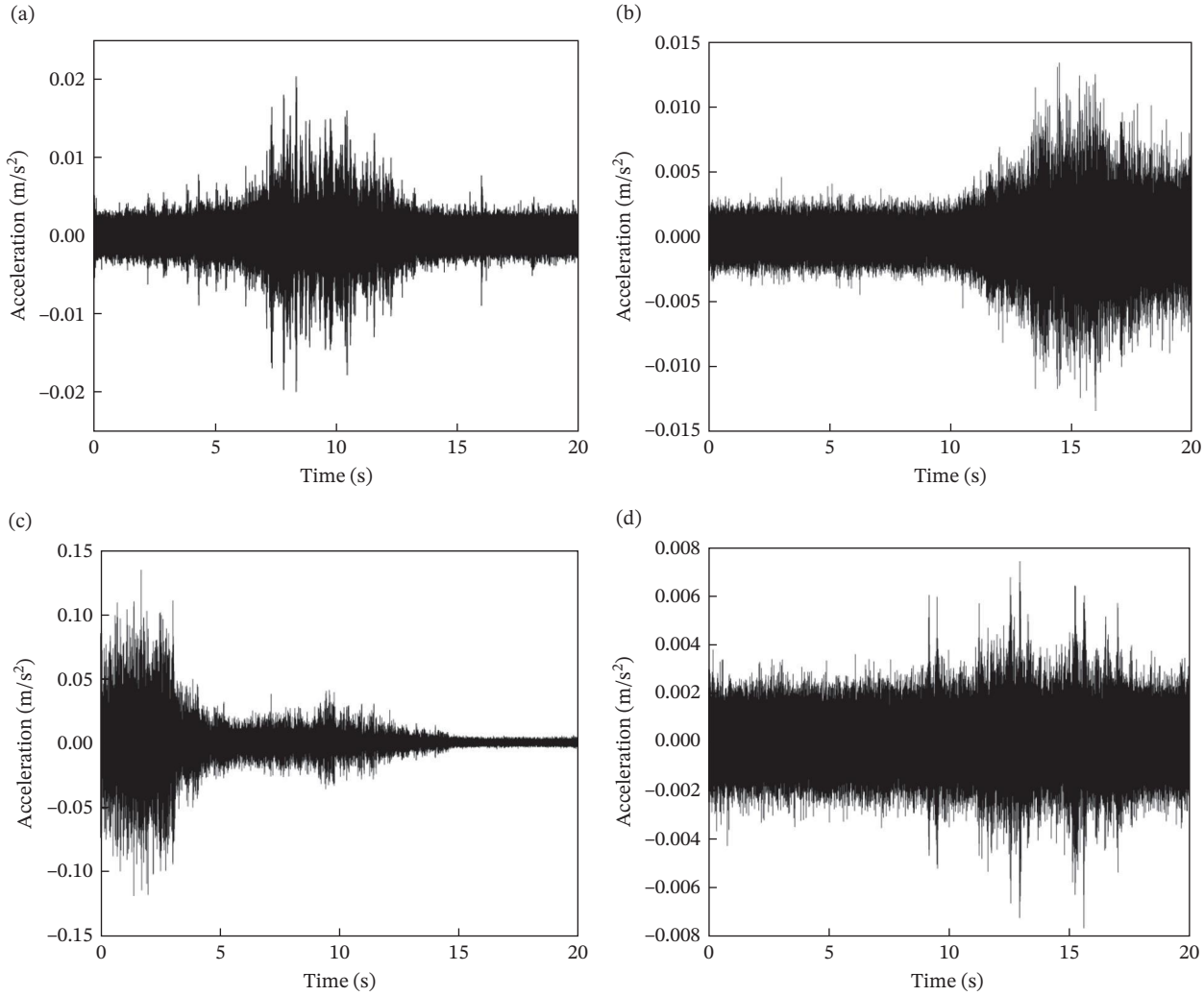


FIGURE 5 | Train vibration signal. (a) p1, (b) p2, (c) p4, and (d) p3.

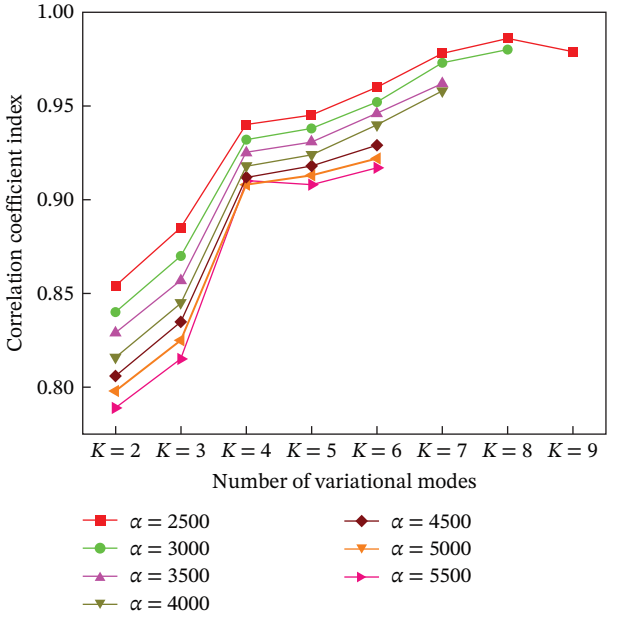


FIGURE 6 | Relevant indicators for different penalty factors.

As shown in Figure 8, the center frequencies of IMF1–8 increase sequentially, and each IMF component represents the spectrum of a different time interval, with no modal aliasing observed. Therefore, when $k=8$ and $\alpha=2500$, it is appropriate to apply the VMD algorithm to the measured signal for noise reduction.

3.3.2 | Time-Frequency Energy Analysis

To identify modes containing effective vibration information, the IMF components undergo Hilbert–Huang transformation (HHT) [28]. The Hilbert spectrum is the most intuitive result obtained from the Hilbert–Huang transform; it reflects the relationship between a signal's time, instantaneous frequency, and amplitude. It is used to analyze how the components of a signal vary over time in order to identify local features. The principle is as follows:

For a real signal x that satisfies the following conditions:

$$\hat{x}(t)=\frac{t}{\pi}\int_{-\infty}^{\infty}\frac{x(\tau)}{t-\tau}d\tau. \tag{12}$$

It can be used to generate an analytical signal as follows:

$$v(t)=x(t)+j\hat{x}(t)=a(t)e^{j\theta(t)}, \tag{13}$$

where $a(t)=[x^2(t)+\hat{x}^2(t)]^{1/2}$, $\theta(t)=\arctan(\hat{x}(t)/x(t))$.

TABLE 2 | The IMF center frequency corresponding to different *K*-values.

K	IMF1	IMF2	IMF3	IMF4	IMF5	IMF6	IMF7	IMF8	IMF9
2	76.75	208.79	—	—	—	—	—	—	—
3	76.69	208.45	332.53	—	—	—	—	—	—
4	76.37	203.25	236.68	340.36	—	—	—	—	—
5	65.14	87.76	203.48	237.27	429.63	—	—	—	—
6	64.94	87.57	203.36	236.72	337.83	430.73	—	—	—
7	64.73	87.09	173.09	205.23	237.74	338.49	430.81	—	—
8	64.69	87.02	**171.66**	**204.07**	**231.69**	**257.81**	341.42	431.01	—
9	3.01	65.21	87.63	202.24	229.92	256.18	329.63	360.60	431.66

Note: When $K = 8$, the number of IMF components with stable center frequencies is the highest.

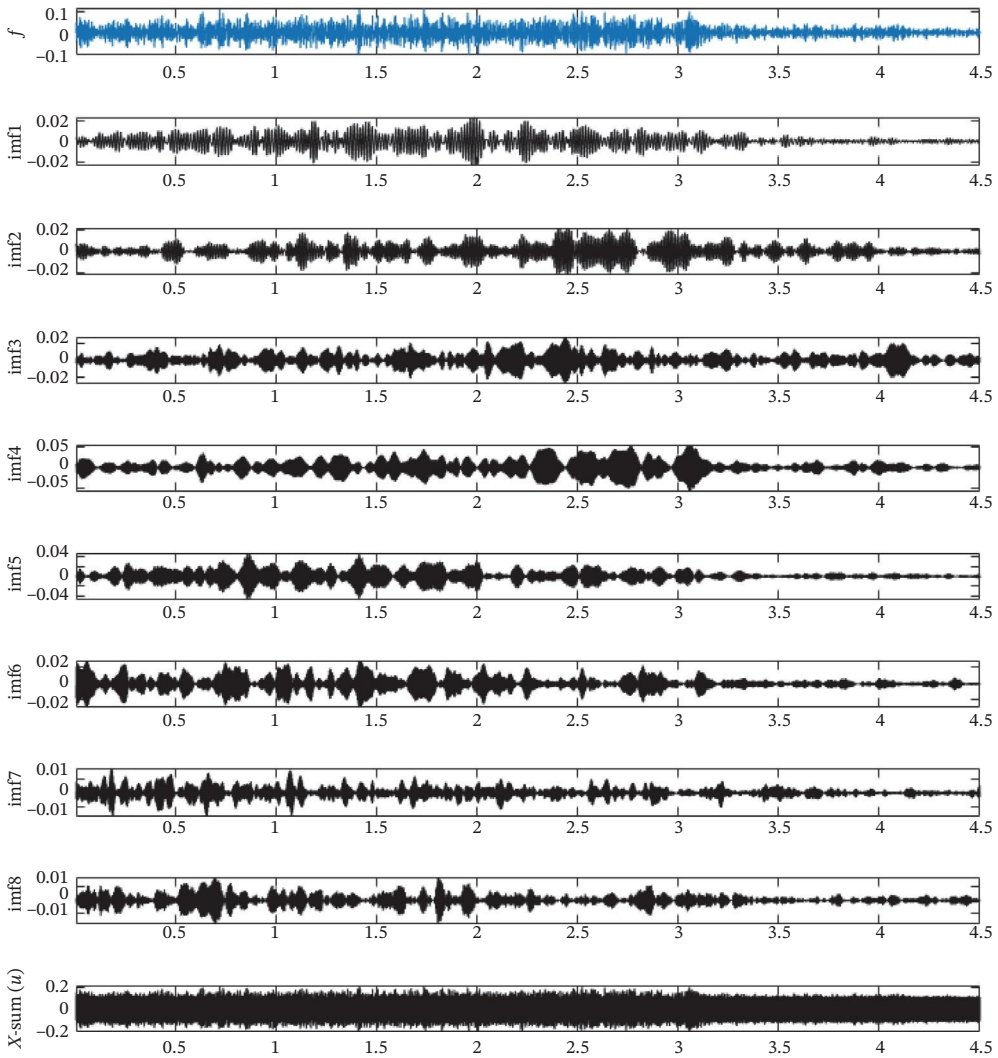


FIGURE 7 | Original signal and eigenmode function.

The instantaneous frequency is given as follows:

$$f(t) = \frac{\omega(t)}{2\pi} = \frac{1}{2\pi}\frac{d\theta(t)}{\mathrm{dt}}. \tag{14}$$

Applying HHT to a vibration signal allows for the identification of the energy distribution of nonstationary noise across multiple frequency bands over time. As shown in Figure 9, the noise is predominantly distributed at both high (>300 Hz) and low (<150 Hz) frequencies, while effective vibration energy is concentrated in the 150–300 Hz frequency band (corresponding to IMF3 to IMF6). The denoised signal retains the key characteristics of the original signal while removing high-frequency noise (>300 Hz) and low-frequency noise (<150 Hz), as illustrated in Figure 10.

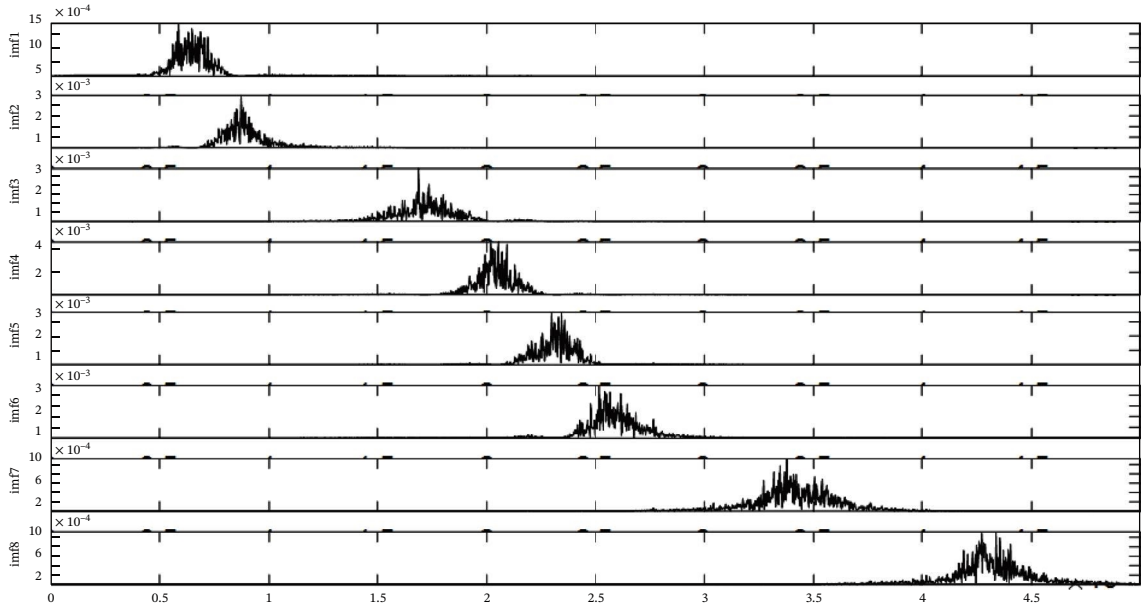


FIGURE 8 | Modal function FFT frequency-amplitude spectrum analysis plot.

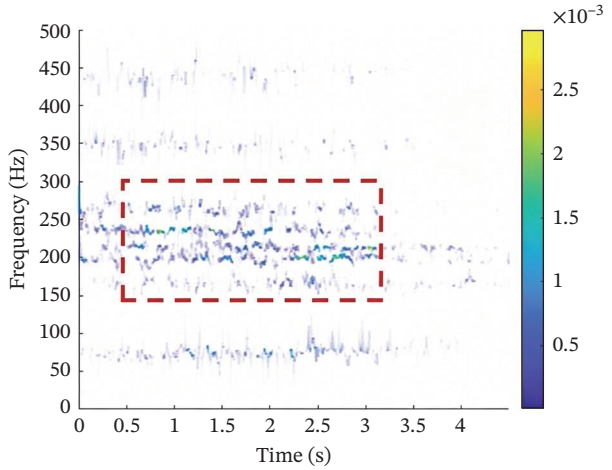


FIGURE 9 | Hilbert spectrum.

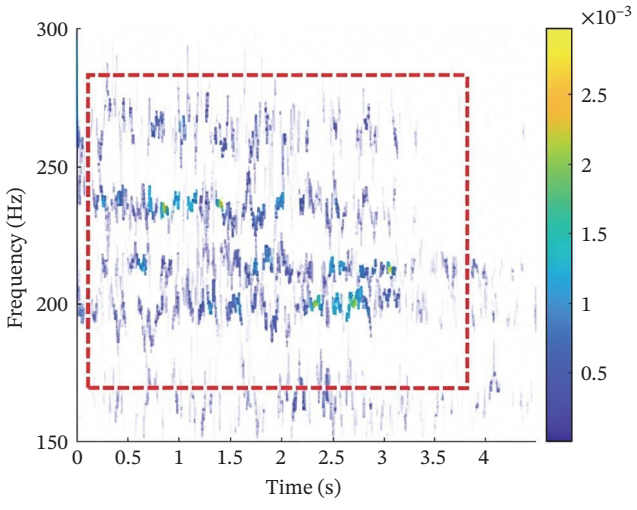


FIGURE 10 | Hilbert spectrum at frequencies 150–300 Hz.

3.3.3 | Analysis of Noise Reduction Results for Different IMF Combinations

Based on this finding, the individual IMF components were recombined and compared with the original signal. Specifically, all components from IMF1 to IMF8 were superimposed to form signal Fs18, and so on. This process ultimately yielded seven reconstruction strategies: Fs18, Fs28, Fs38, Fs48, Fs58, Fs68, and Fs78. Evaluation metrics included mean-squared error, correlation coefficient, and the objective function value, as shown in Figure 11. The metrics exhibit only minor variations across Fs18, Fs28, and Fs38. The significant differences occur starting from Fs48, where the effective frequency components are discarded. This phenomenon is consistent with the Hilbert spectrum observation that the dominant vibration energy is concentrated in

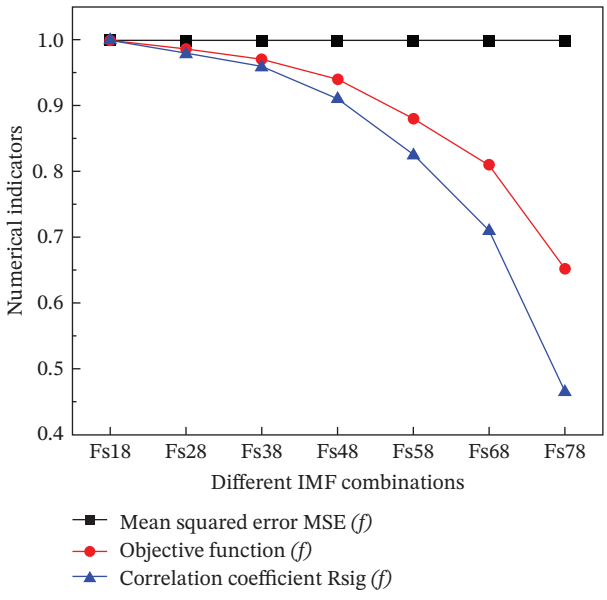


FIGURE 11 | Mean square error, correlation coefficient, and objective function.

IMF3–IMF6. As shown in Figure 12, beyond these effective frequency components, the reconstructed signal loses its fidelity to the original measurements.

4 | Multisource Vibration Superposition Model

4.1 | Principle of Superposition

Under actual engineering conditions, especially when newly constructed subway tunnels cross multiple existing lines, multiple vibration sources are generated. As shown in Figure 13, a newly constructed tunnel passing through two existing lines is affected by two vibration sources, resulting in a vibration superposition effect.

Assuming that there are D vibration sources in the above region, all of which are simplified to simple harmonic vibrations,

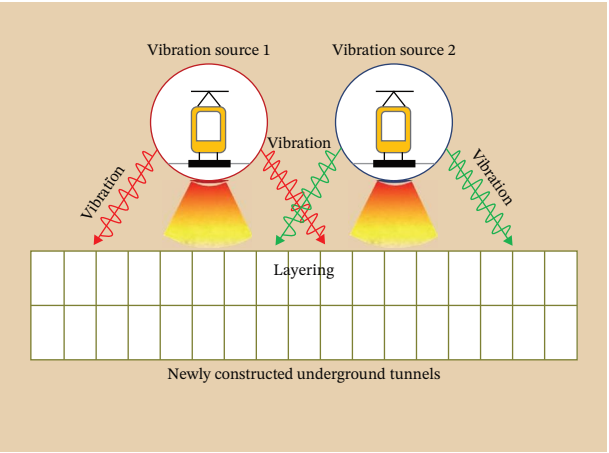


FIGURE 13 | Schematic diagram of dual-source superposition.

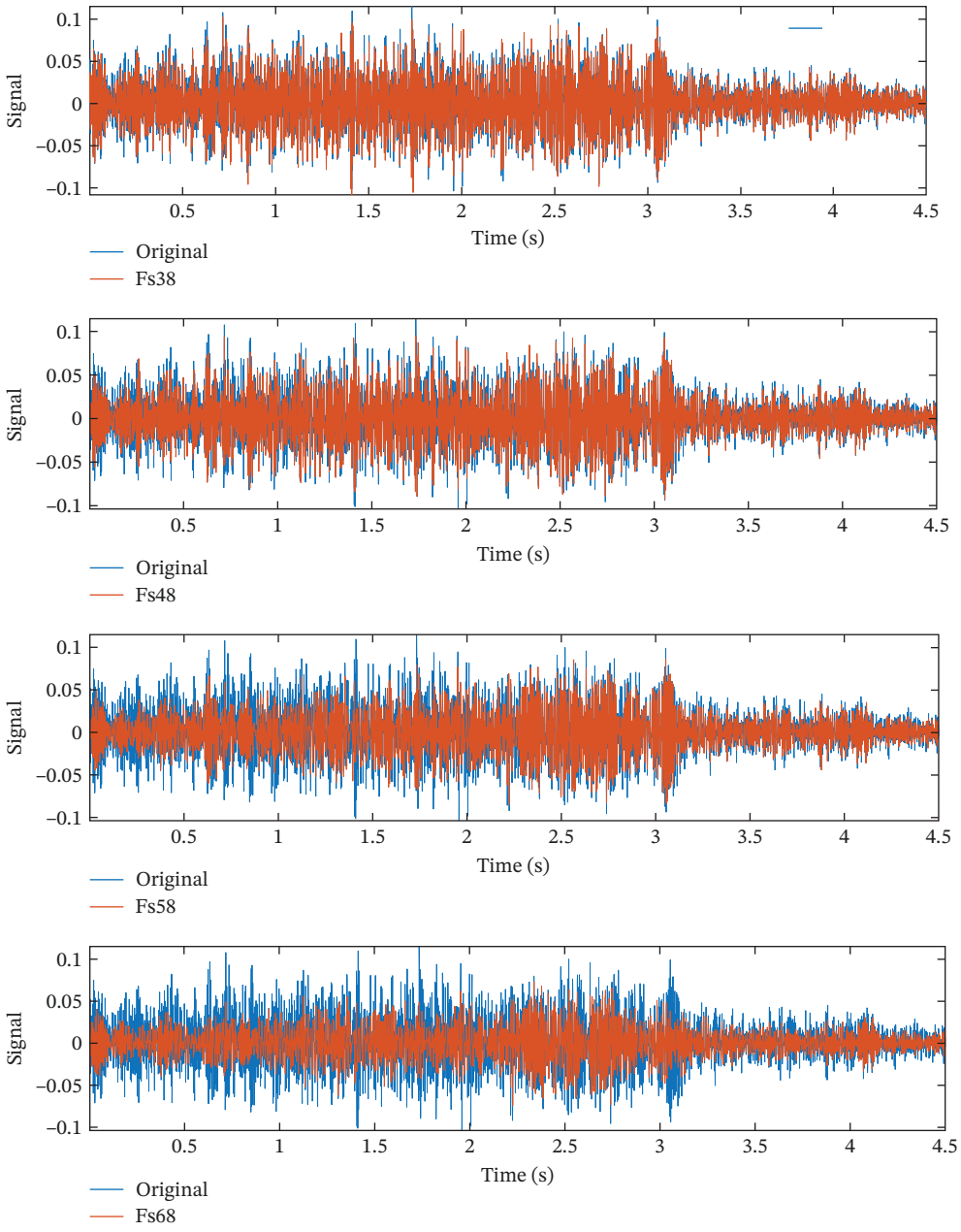


FIGURE 12 | Comparison of different IMF combinations with original data.

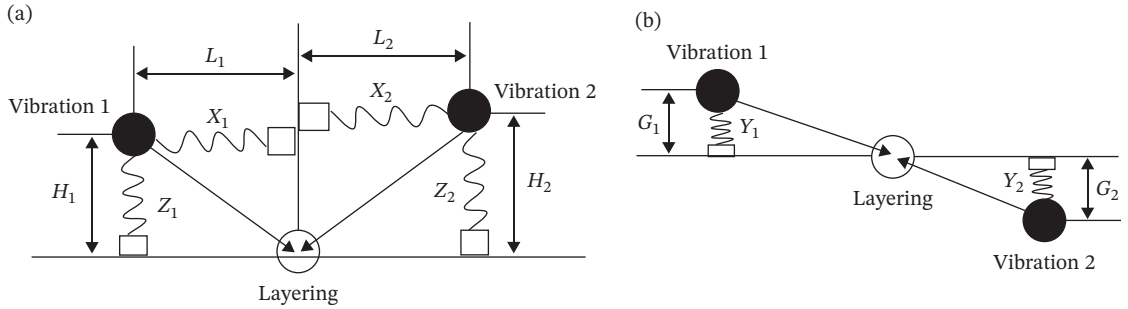


FIGURE 14 | Diagram of the superimposition of different positions. (a) *X* and *Z* and (b) *Y*.

the mathematical expression for the simple harmonic vibration of the i^{th} source is as follows:

$$Q_{\text{ri}}(t) = Q_{\text{ri}}\sin(\omega_i t + \phi_{\text{ri}}), \tag{15}$$

where Q_{ri} is the amplitude after propagation, ω_i is the circular frequency of the pair, and φ_{ri} is the phase.

The vibration synthesis for the above D sources can be expressed as follows:

$$Q_r = \sum_{i=1}^{D} Q_n(t) = \sum_{i=1}^{D} Q_{ri}\sin(\omega_i t + \phi_{\text{ri}}). \tag{16}$$

As shown in Equation (16), the relative position of each vibration source is set to be unchanged at this time, and only the amplitude Q_{ri} and phase φ_{ri} of the vibration source are considered to be uncertain, and the vibration superposition has randomness. In the actual site, the relative position of each vibration source is different for different working conditions. As shown in Figure 14, the superposition of different positions schematic, in the *X*, *Y*, and *Z* direction of the vibration source, and the superposition of the distance corresponding to the position of *L*, *G*, and *H*. Specifically corresponding to a certain direction, the vibration source to reach the superposition of the different distances, the individual vibration source of the superposition of the different effects on the position, which ultimately leads to different vibration superposition effect.

Vibration attenuates during transmission. Therefore, for a single source, damping is considered in the *X*, *Y*, and *Z* directions. Combining with Equation (16), the damping force can be expressed as follows:

$$f_{\text{ri}} = -\gamma\frac{dQ_{\text{ri}}(t)}{\text{dt}}, \tag{17}$$

where f_{ri} is the damping force of the i^{th} vibration source after passing a certain propagation distance ri, and γ is the drag coefficient.

From Newton's second law and damped vibration theory, the equation can be derived as follows:

$$\frac{d^2Q_{\text{ri}}(t)}{\text{dt}^2} = -\omega_0^2 - \eta\frac{dQ_{\text{ri}}(t)}{\text{dt}}, \tag{18}$$

where ω_0 is the intrinsic frequency of the vibration source and η is the damping factor.

Combined with Equation (17),

$$Q_{\text{ri}}(t) = \xi e^{i\omega t+\alpha}, \tag{19}$$

where ξ, α is the effective coefficient.

A quadratic derivation of Equation (19) yields as follows:

$$\frac{d^2Q_{\text{ri}}(t)}{\text{dt}^2} = -\xi\omega^2 e^{i\omega t+\alpha}. \tag{20}$$

Substituting Equation (18) into Equation (20) gives:

$$Q_{\text{ri}}(t) = \xi e^{-\eta t}e^{\pm i\sqrt{\omega_0^2-\eta^2}+\alpha}. \tag{21}$$

Vibration in the propagation process is bound to have attenuation, assuming that the *X*, *Y*, and *Z* direction attenuation is 0 when the propagation distance is *s*, it can be seen that when Li, Gi, and Zi < s, there will be a vibration response, as can be seen from Equation (21).

If, then Equation (21) holds, and can be obtained as follows:

$$Q_{\text{ri}}(t) = \xi e^{-\eta t}\sin\left[\left(\sqrt{(\omega_0^2-\eta^2)}\right)t+\alpha\right]. \tag{22}$$

At this point, ξ, δ, α are constant and the amplitude decays with increasing propagation distance. Taking the *X*-direction as an example, for two sources with propagation distances s_1 and s_2, the total superposition length in the *X*-direction is $(s_1+s_2)-(L_1+L_2)$, provided that $L_1 < s_1$ and $L_2 < s_2$.

The vibration synthesis of the above two vibration sources can be expressed as follows:

$$Q_r = Q_{r1}\sin(\omega_1 t + \phi_{r1}) + Q_{r2}\sin(\omega_2 t + \phi_{r2}). \tag{23}$$

In FLAC3D, custom functions are developed using the built-in FISH language to apply multisource vibration loads that account for attenuation. A detailed workflow diagram is shown in Figure 15.

4.2 | Numerical Simulation

According to the engineering geological investigation report, the strata are simplified into four layers, as shown in Figure 16. To eliminate the influence of the soil far-field boundaries on the calculation results, the existing Line 10 tunnel and Line 14 are each positioned 20 m from the boundaries on both sides. The new tunnel is located 42 m from the boundaries on both sides, with the model base positioned 42 m from the new tunnel. The model

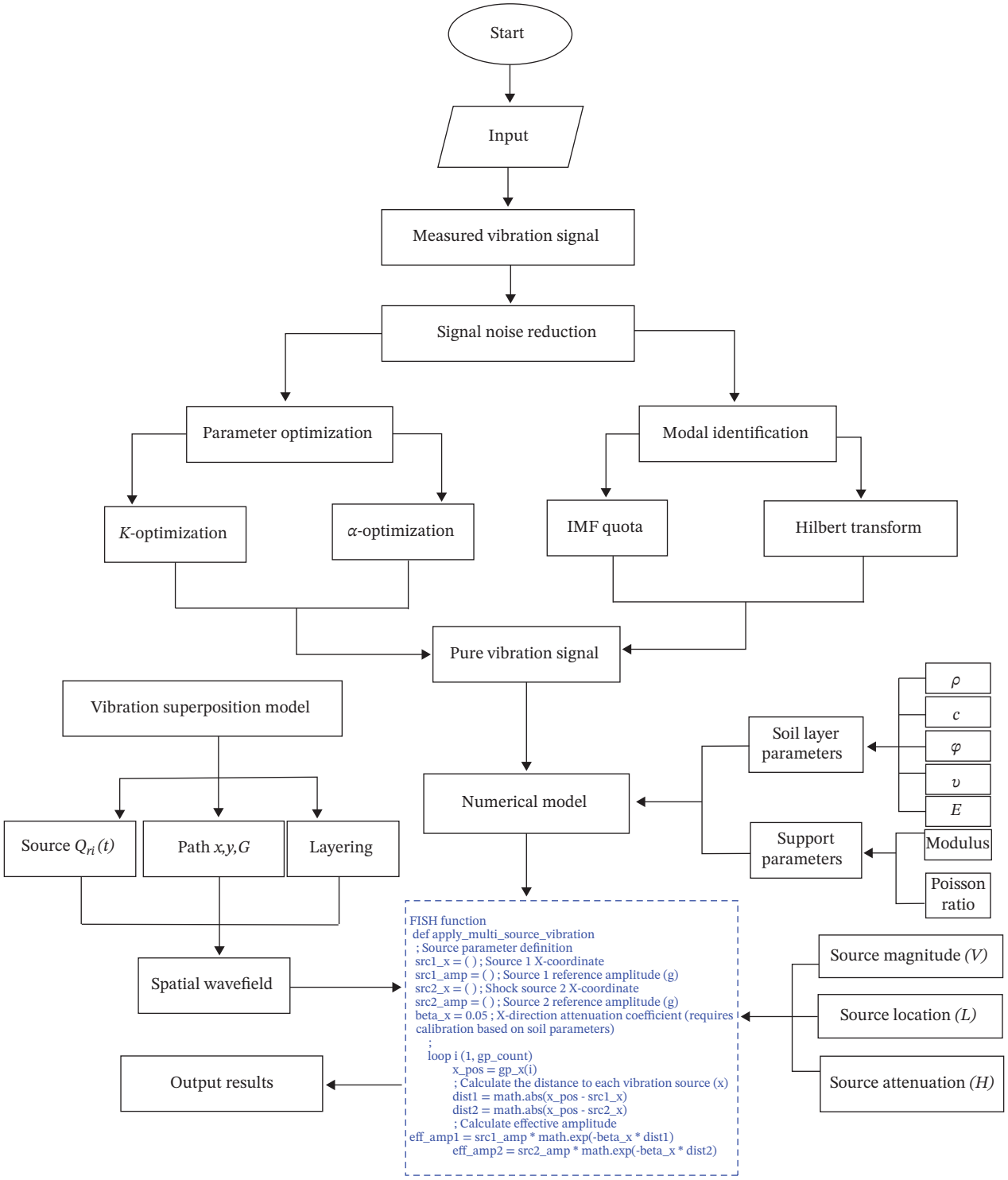


FIGURE 15 | Workflow diagram.

dimensions are: $x^* y^* z = 180\,\text{m} \times 100\,\text{m} \times 90\,\text{m}$. The model boundaries are set as free-field boundaries (lateral boundaries) to simulate an infinite domain, with a fixed boundary at the bottom ($z = 0$). The initial ground stress field considers only the effect of gravity.

To verify that wave reflections from the lateral boundaries do not significantly affect the computed dynamic response, a boundary sensitivity analysis was conducted. As shown in Table 3, increasing the model width from 180 to 240 m changed the peak acceleration by −4.3% at A4 and −3.7% at C2. Further increasing the width to 300 m resulted in additional changes of less than 2% (cumulative −5.9% at A4 and −4.9% at C2). These variations are within 6%, confirming that the baseline model width of 180 m provides sufficient isolation from boundary effects.

The soil is modeled using the Mohr–Coulomb constitutive model, which is widely used in geotechnical engineering because it can reasonably describe the shear failure behavior of soils, its parameters are readily obtainable, and it offers high computational

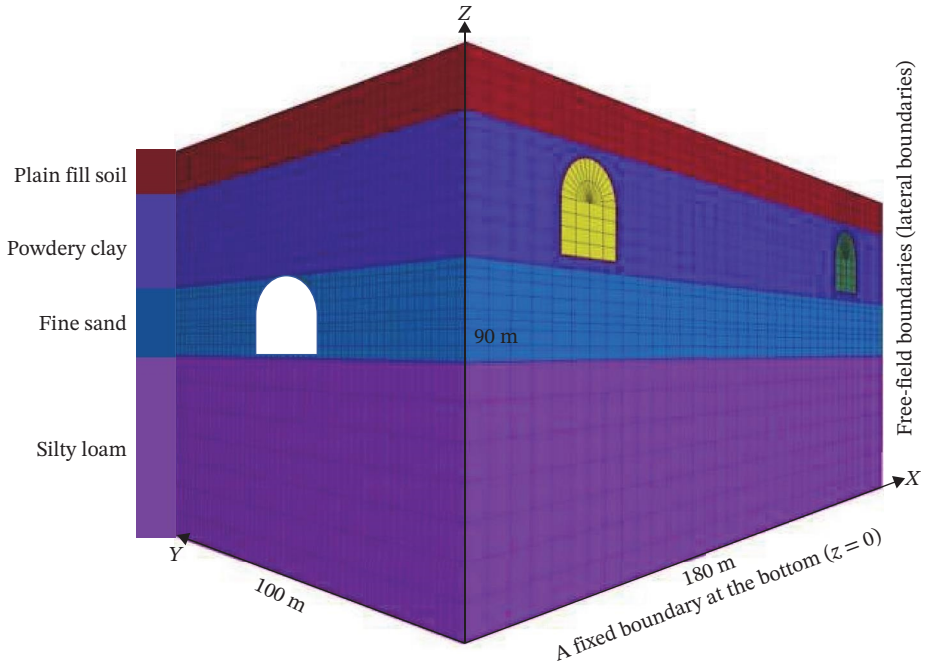


FIGURE 16 | Numerical model.

TABLE 3 | Boundary sensitivity analysis results (dual-line, 40 km/h).

Model width (m)	Distance from existing line to boundary (m)	Peak acceleration at A4 (m/s^2)	Change relative to baseline (A4)	Peak acceleration at C2 (m/s^2)	Change relative to baseline (C2)
180 (baseline)	20	0.187	—	0.163	—
240	50	0.179	−4.3%	0.157	−3.7%
300	80	0.176	−5.9%	0.155	−4.9%

TABLE 4 | Simplified soil parameters.

Name	ρ (g/cm^3)	c (KPa)	ϕ (°)	υ	E (MPa)
Plain fill	1.87	8.0	10.0	0.30	3.0
Clayey Silt	2.05	0.0	28.0	0.32	20.0
Silty fine sand	2.01	30.0	22.0	0.27	11.0
Silty clay	2.28	35.0	24.0	0.36	16.0

Note: c, cohesion; φ, internal friction angle; ν, Poisson's ratio; E, elastic modulus.

TABLE 5 | Structural calculation parameters.

Serial number	Name	Elastic modulus (MPa)	Poisson's ratio	Density (kg/m^3)
1	Primary concrete C25	28,000	0.20	2400
2	Main structure concrete C30	30,000	0.20	2500

efficiency, suitable for dynamic response analysis where plastic deformation is considered. The lining structure is modeled as elastic since concrete linings typically remain in the elastic stage under train-induced vibration loads (stress levels far below the compressive strength), and the elastic model provides stable convergence and sufficient accuracy for engineering purposes. Material parameters were determined based on the investigation report and laboratory tests as shown in Tables 4 and 5.

Rayleigh damping is employed, where the damping matrix is given as follows:

$$[C] = \alpha[M] + \beta[K]. \tag{24}$$

The coefficients α and β are determined from the target damping ratio $\xi = 0.05$ (typical for soil dynamic problems) and the dominant frequency range.

In dynamic analysis, differences in model conditions can lead to distortions in wave propagation during numerical simulations; both the frequency of the input wave and the wave velocity characteristics of the system affect the accuracy of wave propagation. To accurately describe wave propagation in the model, the dimensions of the model elements must be less than 1/10–1/8 of the wavelength corresponding to the highest frequency of the input wave.

The overall equation of motion for dynamic analysis is expressed as follows:

$$[M]\{\ddot{u}\} + [C]\{\dot{u}\} + [K]\{u\} = \{F(t)\}. \tag{25}$$

Using the vibration signal denoised by the VMD algorithm as the reference waveform, the FISH command is invoked to combine the reference waveform with a multisource superposition model accounting for spatial attenuation. This combined model is then applied as a dynamic load within the FLAC3D model. The specific computational steps are illustrated in Figure 17.

As shown in Figure 18a, the monitoring layout along the excavation direction includes seven monitoring planes (A1–A7) for the existing Line 10 underpass section and seven monitoring planes (B1–B7) for the existing Line 14 underpass section, with each plane spaced 4 m apart. To investigate vibration superposition effects, three monitoring surfaces (C1–C3) were established at nonunderpass locations, spaced 20 m apart. As shown in Figure 18b, monitoring points (P1–P8) were installed on the roof, side walls, and floor of both upper and lower pilot tunnels perpendicular to the excavation direction.

When two trains on existing lines pass through the underpass under construction at different times, they produce distinct vibration responses in the newly constructed tunnel. Key factors considered include whether the existing lines are in operation, the spacing between the two existing lines, and the distance between the existing lines and the new tunnel. Based on research, operating conditions 1–21 were selected for simulation, as shown in Figure 19 and Table 6, and analyzed.

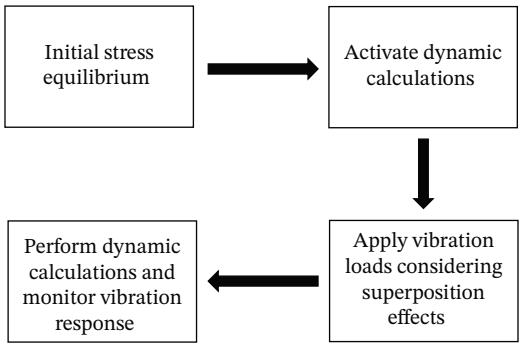


FIGURE 17 | Power calculation procedure.

5 | Results and Discussion

5.1 | Method Validation and Comparative Analysis

As shown in Figure 20, by comparing the vibration acceleration at the A4 monitoring section with the frequency spectrum at point P1, it was found that the vibration response after applying the superimposed noise reduction coupling simulation was closer to the measured values. In contrast, the simulation results obtained by directly substituting the measured signals without noise reduction showed a larger discrepancy from the actual measurements. For the proposed method (VMD-denoised + superposition), the peak acceleration error at point P1 is 6.8% relative to field measurements, compared to 18.6% for the undenoised coupled simulation. The MSE over the 20 s duration is 0.043 m/s^2 for the proposed method versus 0.112 m/s^2 for the undenoised simulation, validating the effectiveness of the superimposed noise reduction coupling simulation method.

5.2 | Effect of Vibration Source Intensity

As shown in Figure 21, the greater the vibration source intensity, the larger the peak acceleration. The maximum peak acceleration occurs at points A4 and B4, while the minimum peak acceleration is observed at point C2, which is the midpoint between the two existing tracks. The peak acceleration curve exhibits

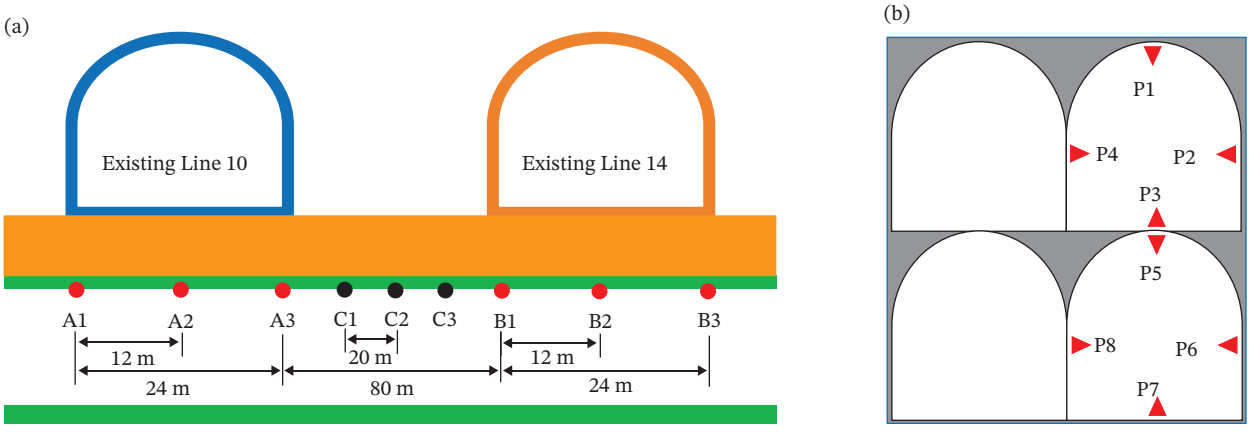


FIGURE 18 | Numerical simulation monitoring layout. (a) Excavation direction and (b) vertical excavation direction.

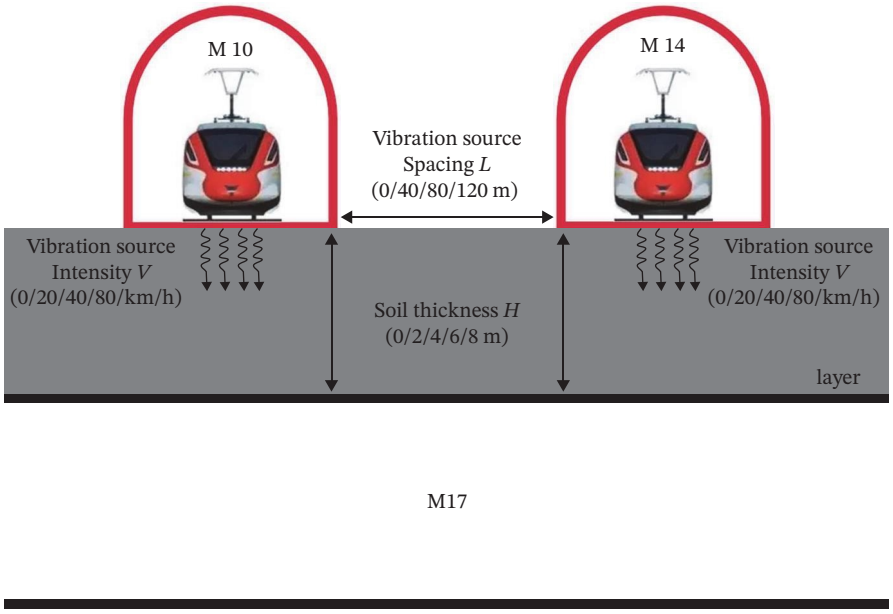


FIGURE 19 | Schematic illustration of simulation scenarios.

TABLE 6 | Simulation conditions.

Condition	Line 10	Line 14	Distance between two existing lines, L (m)	Soil thickness, H (Line 10) (m)	Soil thickness, H (Line 14) (m)	Train speed (km/h)
1	Pass	No	80	2	2	20
2	Pass	No	80	2	2	40
3	Pass	No	80	2	2	80
4	No	Pass	80	2	2	20
5	No	Pass	80	2	2	40
6	No	Pass	80	2	2	80
7	Pass	Pass	80	2	2	20
8	Pass	Pass	80	2	2	40
9	Pass	Pass	80	2	2	80
10	Pass	Pass	0	2	2	80
11	Pass	Pass	40	2	2	40
12	Pass	Pass	120	2	2	40
13	Pass	No	40	2	2	40
14	Pass	No	120	2	2	40
15	Pass	Pass	80	0	0	40
16	Pass	Pass	80	4	4	40
17	Pass	Pass	80	6	6	40
18	Pass	Pass	80	8	8	40
19	Pass	No	80	4	4	40
20	Pass	No	80	6	6	40
21	Pass	No	80	8	8	40

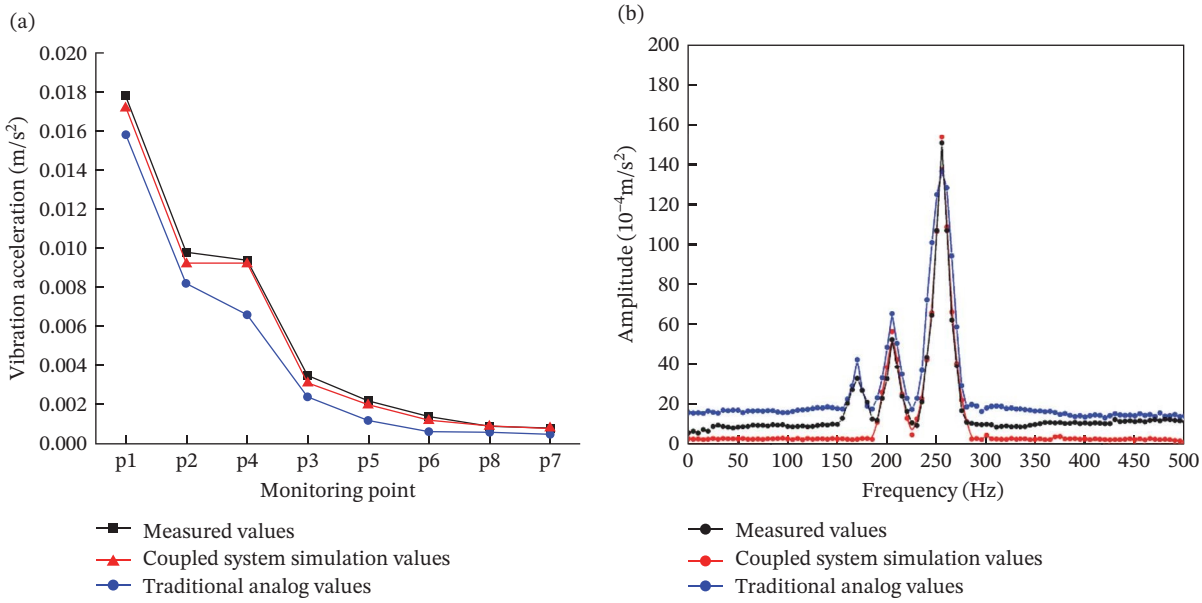


FIGURE 20 | Comparative verification of monitoring section A4. (a) Acceleration at monitoring section A4 and (b) frequency at point P1.

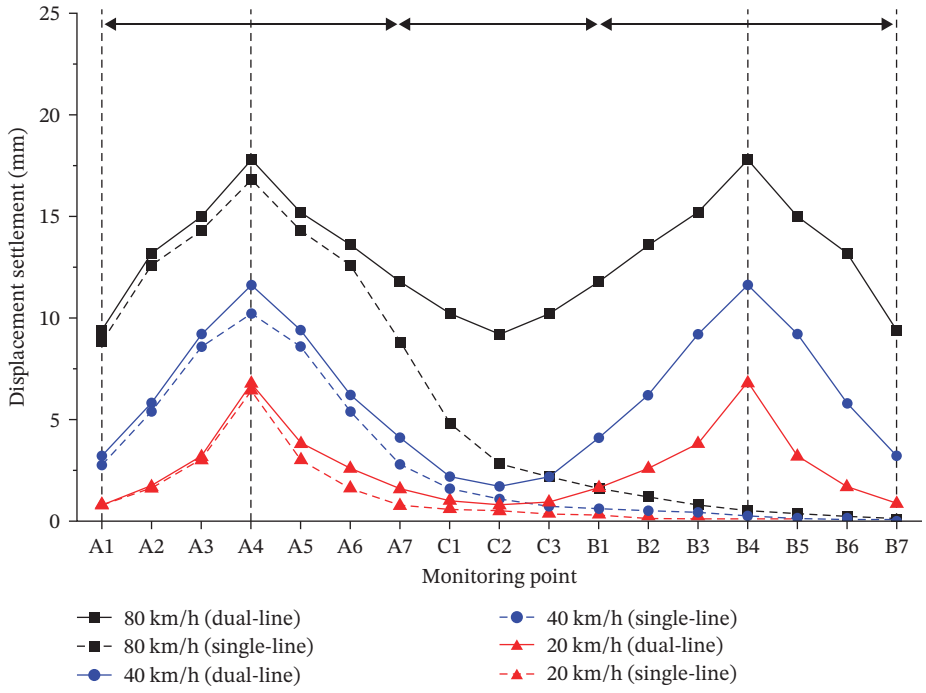


FIGURE 21 | Peak vibration acceleration of P1.

symmetry about C2. When the vibration source intensity is high, the peak acceleration at the same monitoring point is greater during the double-track operation than during the single-track operation. This indicates that the two vibration sources interact with each other, resulting in vibration superposition.

As shown in Figure 22, when the train speed is 80 km/h and existing double-track trains operate simultaneously, the maximum principal stress occurs in the section of the lower new tunnel crossing beneath the existing line. The smallest value of the maximum principal stress was observed at a train speed of 20 km/h. Since the crossing section features an intersecting structure, the concentrated distribution range of maximum principal stress is primarily centered around the crossing points A4 and B4. A larger horizontal spacing between trains results in a broader area of maximum principal stress concentration. Compared to the operating conditions of a single existing train, the area of maximum principal stress concentration is the largest when the train speed is 80 km/h.

As shown in Figure 23, the frequency variations at points A4, C1, and C2 were studied, with a dominant frequency of 255 Hz. A larger vibration source (higher train speed) results in a greater amplitude at the dominant frequency. For point C2, a larger

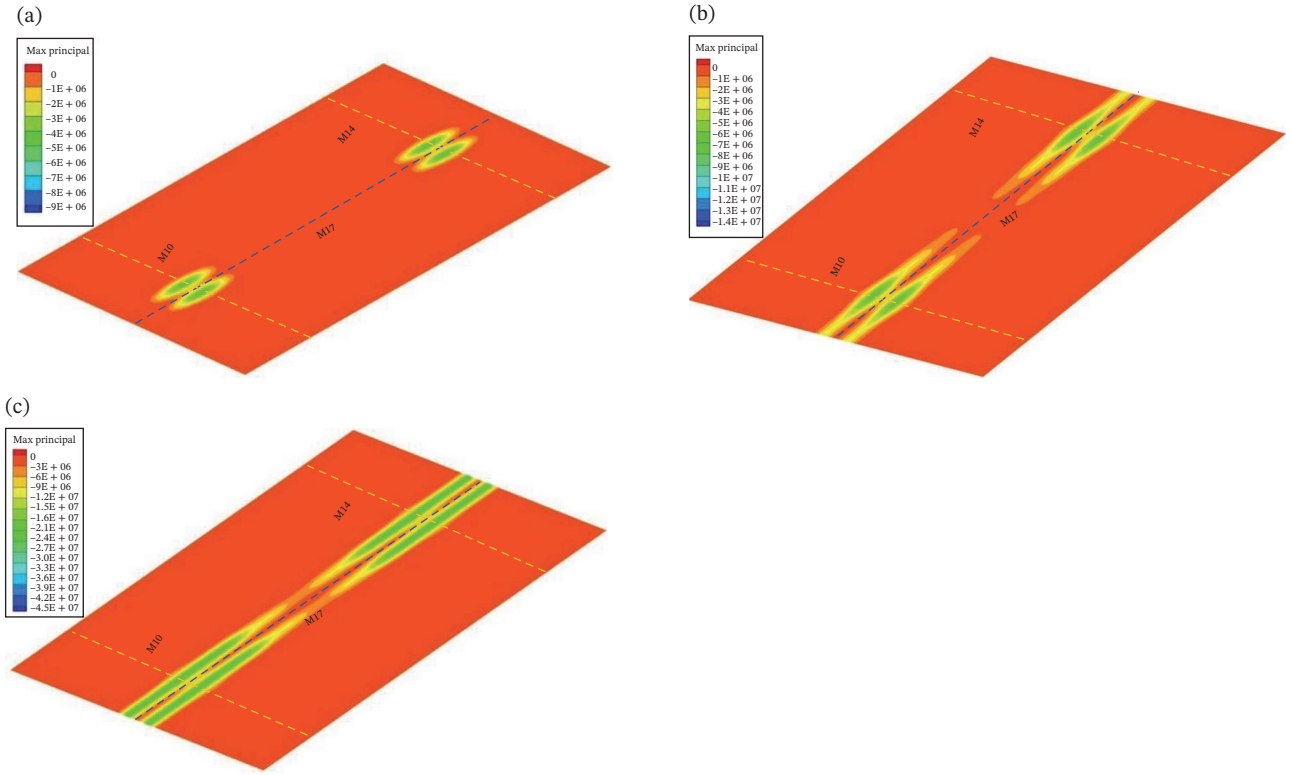


FIGURE 22 | Contour map of maximum principal stress distribution under different passing conditions. (a) 20 km/h, (b) 40 km/h, and (c) 80 km/h.

vibration source generates an additional amplitude peak near 170 Hz, and this amplitude increases with the size of the vibration source. For point A4, when the train speed increases from 20 to 40 km/h, a new amplitude peak emerges near 205 Hz, indicating that new frequency components are indeed introduced at this location. When the speed further increases to 80 km/h, the 205 Hz peak amplitude increases by approximately 35%. Comparing points C1 and C2, the amplitude at the primary frequency (255 Hz) is smaller at C2 than at C1, but the amplitude at nonprimary frequencies (170 Hz) is larger at C2. This indicates that the dual-line trains interact with each other, with the greatest influence occurring at point C2.

5.3 | Effect of Vibration Source Position

As shown in Figure 24, monitoring the roof position P1 reveals that the peak vibration acceleration at each monitoring location is highest when the distance L between the two vibration sources is 40 m, followed by $L = 80$ m and lowest at $L = 120$ m. This indicates that the closer the distance between vibration sources, the stronger the vibration response. Within the underpass section at $L = 120$ m, the trend of acceleration peak variation is remarkably gradual, with the highest vibration acceleration peaks observed at the central points A4 and B4.

As shown in Figure 25, when the horizontal distance between the existing double tracks is $L = 40$ m and trains on both tracks operate simultaneously, the maximum principal stress occurs in the section of the lower new tunnel passing beneath the existing tracks. The maximum principal stress is minimized when the horizontal distance reaches 120 m. As the horizontal distance between the existing double tracks gradually increases, the influence range of the maximum principal stress progressively decreases. When the horizontal distance is 120 m, the maximum principal stress's influence range is primarily concentrated at the section where the train passes beneath the existing tracks.

As shown in Figure 26, the vibration superposition rate at monitoring point P1 along the excavation direction is the highest at point C2, reaching 54.6%. This indicates that the center point (C2) between the two existing lines is most affected by vibration superposition. This demonstrates that the smaller the horizontal distance L between the two existing lines, the larger the area affected by the superimposed response. When the horizontal distance L between the two existing lines changes from 120 to 80 m, the increase in the affected area is less than when it changes from 80 to 40 m, indicating that the range of superimposed influence is limited.

5.4 | Vibration Transmission Attenuation

As shown in Figure 27, monitoring at the roof position P1 indicates that the peak vibration acceleration at each monitoring location is highest when the soil layer thickness H between the existing line and the new tunnel is 2 m and lowest when $H = 8$ m. This demonstrates that the closer the existing line is to the newly constructed tunnel, the stronger the vibration response. Within the underpass range of the four operating conditions, the peak vibration acceleration trends are similar, with the highest peaks occurring at the underpass centers A4 and B4. Outside the underpass range, the peak vibration acceleration trend at $H = 2$ m is steeper. Overall, the influence of soil layer thickness on the vibration response shows a decreasing trend, with less vibration transmitted to the lower excavated section when $H > 4$ m.

As shown in Figure 28, the vibration superposition rate at monitoring points along C2 is the highest at P1, with the deepest downward transmission reaching only P3. The smaller the vertical

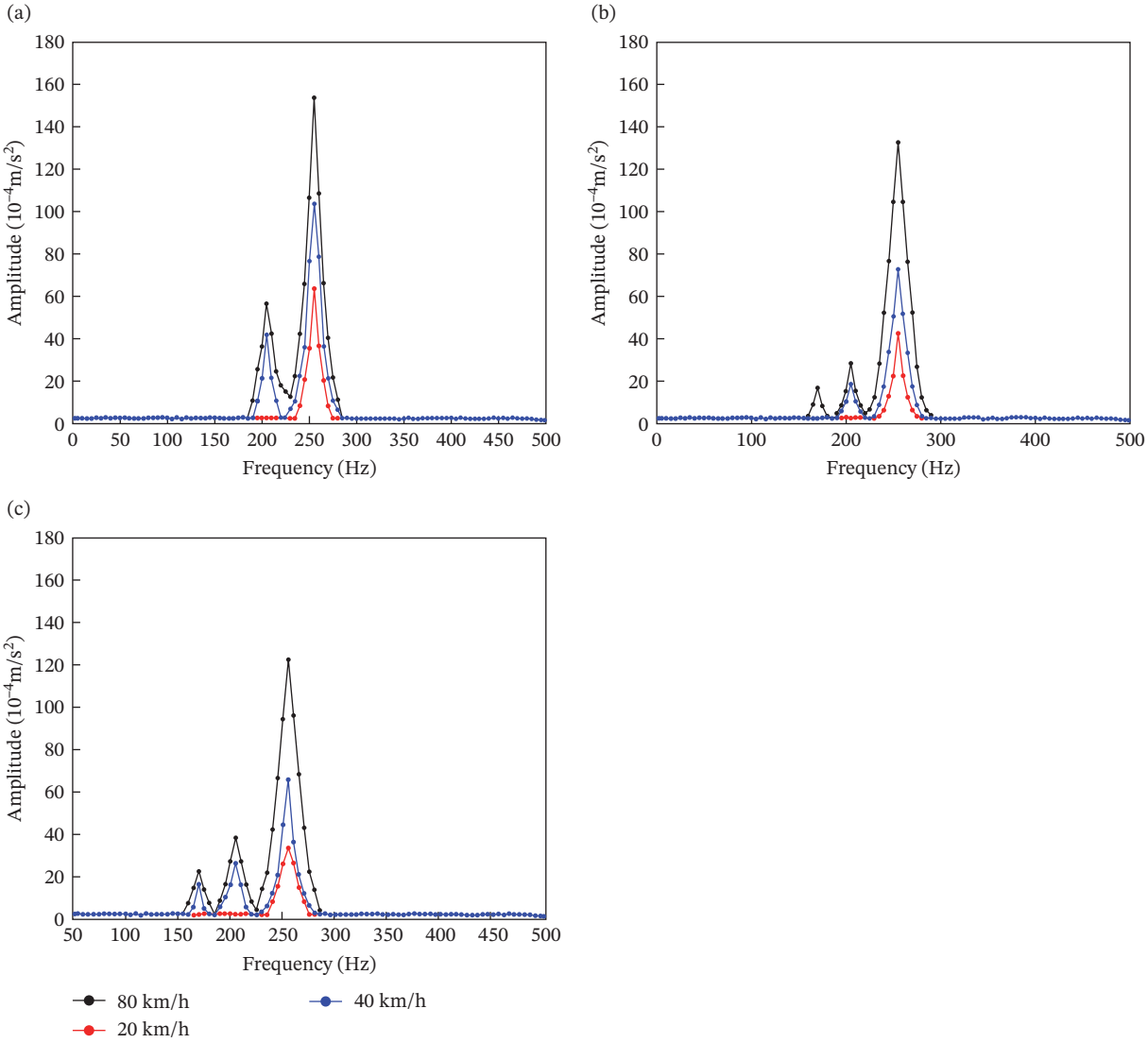


FIGURE 23 | Frequency spectrum diagrams for different vibration source sizes. (a) A4, (b) C1, and (c) C2.

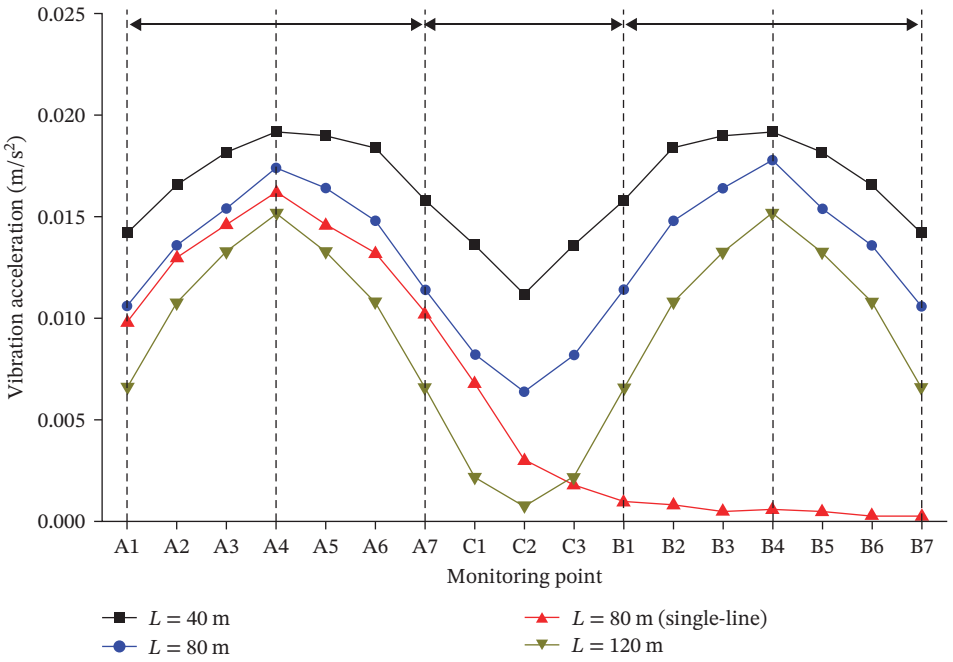


FIGURE 24 | Peak vibration acceleration at point P1.

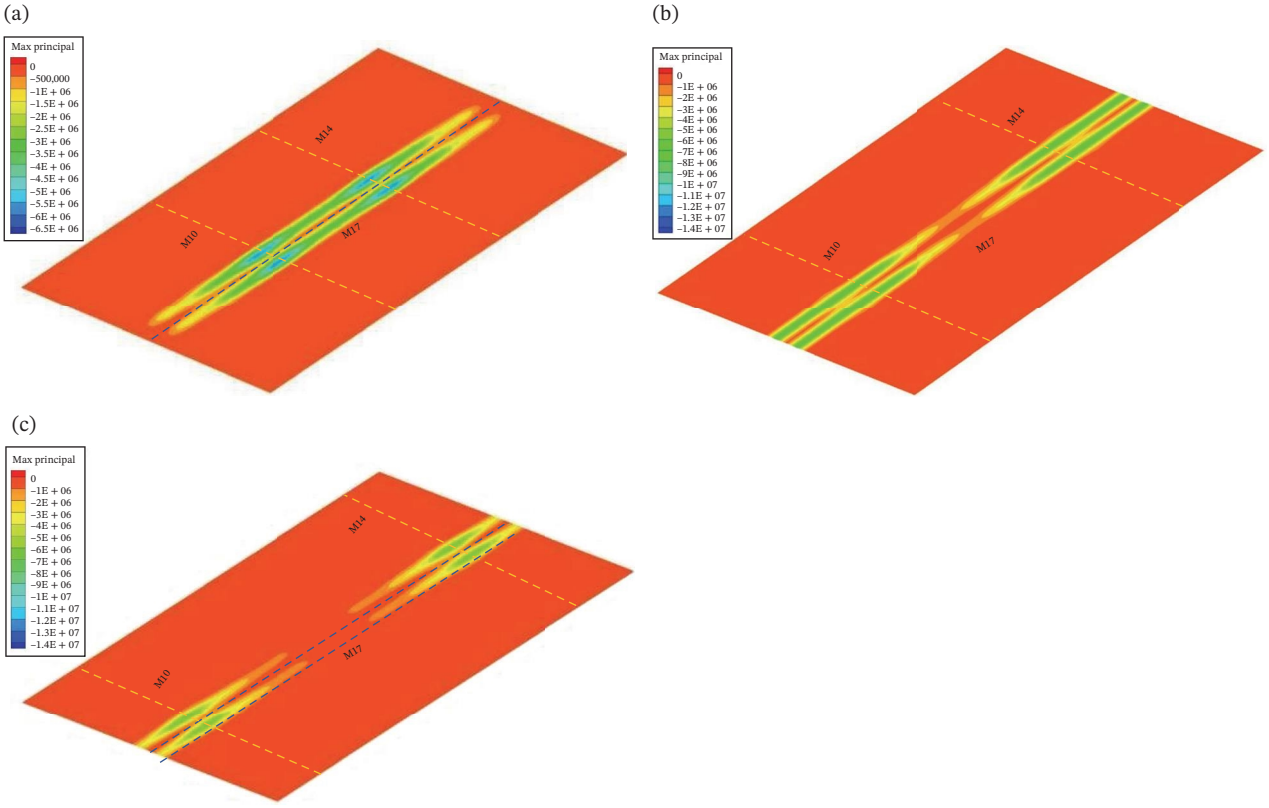


FIGURE 25 | Contour map of maximum principal stress at different source locations. (a) 40 m, (b) 80 m, and (c) 120 m.

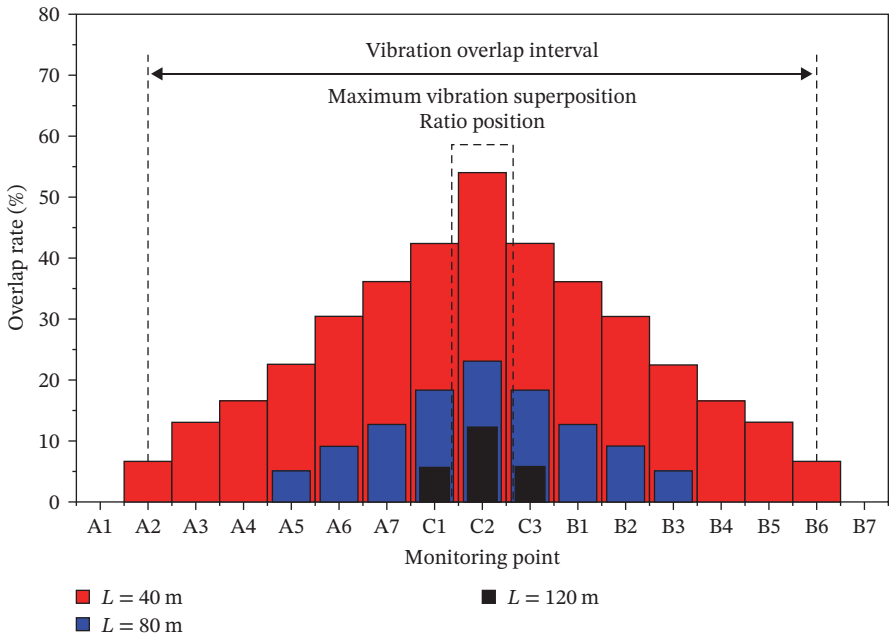


FIGURE 26 | Maximum overlap rate at P1.

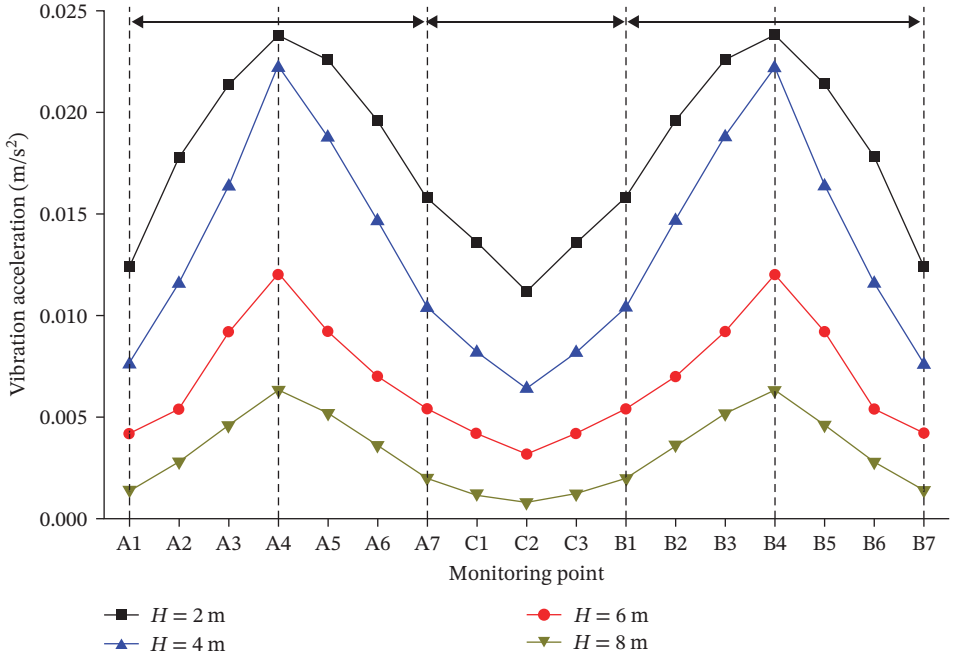


FIGURE 27 | Peak acceleration variation curve at point P1.

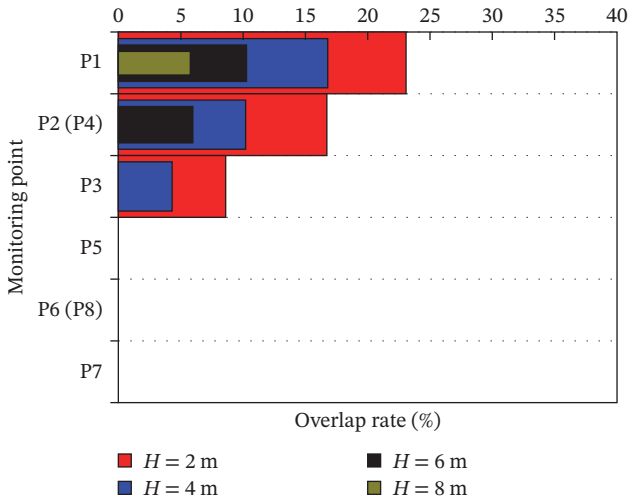


FIGURE 28 | Maximum overlap rate at C2 point.

distance H between the existing line and the newly constructed tunnel, the larger the area affected by the superposition response. This indicates that only the upper pilot tunnel is impacted by vibration superposition.

6 | Conclusions

Tunneling through existing double-track lines during new tunnel construction has become increasingly common in practical engineering projects. This paper investigates the new tunnel of Beijing Subway Line 17 at Shilihe Station, which passes beneath the existing Lines 10 and 14. Regarding the dynamic response of new tunnels traversing existing double-track lines, the following conclusions were drawn:

1. A VMD-based vibration signal denoising process was established. By optimizing key VMD parameters ($K = 8$, $\alpha = 2500$), noise and useful signals were effectively separated, yielding high-fidelity vibration input signals.
2. A multisource vibration superposition model was constructed in FLAC3D. Based on the vibration superposition theory, a superposition formula accounting for propagation attenuation was derived. Precise application of multisource vibration loads was achieved in FLAC3D through FISH programing.
3. When both existing lines were in operation, the vibration superposition effect was most pronounced at point C2. The measured superposition value was not a simple sum of the vibration responses from the two independent sources at this location; instead, the two sources interacted with each other.
4. Comparing the horizontal spacing L between the two existing lines and the vertical distance H between the existing lines and the excavated section indicates that the superposition influence is limited in scope. Analyzing the superposition rates at various monitoring points at C2 reveals that the highest vibration superposition rate occurs at the roof point P1. The superposition rate decreases to 17.3% at P2 (P4) and 8.6% at P3. Using a threshold of 10% to define superposition, only the roof (P1) and upper side walls (P2) are significantly affected, with the deepest downward transmission reaching only P3. This confirms that the vibration superposition effect is primarily confined to the crown of the excavated section.
5. The findings presented above are derived from a specific case study (Beijing Subway Line 17 crossing Lines 10 and 14) with particular geological conditions (silty clay and sandy strata), tunnel geometries (horseshoe cross-section, 2.25 m clearance), and operational parameters (train speeds 20–80 km/h). While the proposed methodological framework (VMD denoising + multisource superposition + FLAC3D simulation) is general and transferable,

the quantitative results are site-specific. Soil stiffness and damping characteristics influence wave propagation and attenuation rates, tunnel depth and clearance distance govern the degree of source–receiver coupling, train type and track condition determine the frequency components of the signal source, and the relative alignment of existing and new tunnels may affect the magnitude of vibration superposition effects. Future work should systematically investigate the sensitivity of superposition effects to these parameters through parametric studies.

Author Contributions

Conceptualization, Methodology, Validation, Formal analysis: Yunsi Liu and Yueyuan Huang. Software: Yueyuan Huang and Yuxiao Wu. Resources: Yunsi Liu. Data curation: Yueyuan Huang and Yuxiao Wu. Writing – original draft: Yueyuan Huang and Yuxiao Wu. Writing – review and editing: Yunsi Liu. Supervision: Yunsi Liu. Project administration: Yunsi Liu. Funding acquisition: Yunsi Liu.

Funding

This research was funded by the National Natural Science Foundation of China (Grant 52378396).

Disclosure

All authors have read and agreed to the published version of the manuscript.

Consent

The authors have nothing to report.

Conflicts of Interest

The authors declare no conflicts of interest.

Data Availability Statement

Data are contained within the article.

References

1. J. Dong, F. Xu, Q. Zhang, et al., "Study on Vibration Characteristics of Fine Breccia Soil Subgrade Reinforced With a New Prestressed Structure Under Train Cyclic Loading," *Construction and Building Materials* 397, no. 15 (2023): 132364.

2. J. Li, Y. Cao, F. Chen, and Y. Lin, "Cumulative Effects of Cyclic Train Loading on Strains in Reinforced Soils Around Tunnels," *Soil Dynamics and Earthquake Engineering* 187 (2024): 108994.

3. R. Heidary, M. Esmaeili, and M. Gharouni Nik, "Effects of Train Operational Parameters on Ground-Borne Vibrations Induced by Twin Metro Tunnels," *International Journal of Rail Transportation* 9, no. 2 (2021): 144–156.

4. J. Chen, S. Hou, B. Zheng, et al., "Train-Induced Vibration and Structure-Borne Noise Measurement and Prediction of Low-Rise Building," *Buildings* 14, no. 9 (2024): 2883.

5. C. He and S. Zhou, "Ground Vibrations Induced by the Passage of Double-Line Trains in Underground Tunnels," *Soil Dynamics and Earthquake Engineering* 165 (2023): 107719.

6. J. Zhang, Q. Yan, K. Yang, and M. Sun, "Experimental Modeling of Adjacent Parallel Shield Tunnels Subjected to Train-Induced Vibration Loads," *Proceedings of the Institution of Mechanical Engineers, Part F: Journal of Rail and Rapid Transit* 235, no. 9 (2021): 1132–1142.

7. Z. Wang, L. Zhang, Z. Ren, J. Mo, L. Yang, and K. Wang, "Friction and Vibration Behaviours of High-Speed Train Brake System Excited by Wheel Flats," *International Journal of Rail Transportation* 12, no. 3 (2024): 458–475.

8. L. Wu, X. Zhang, F. Kuang, J. Sui, Z. Xilong, and H. Guo, "Dynamic Characteristics of Adjacent Tunnel and Surroundings Under the Vibration of Trains in the First Tunnel With Different Buried Depths," *Arabian Journal for Science and Engineering* 46, no. 5 (2021): 5105–5119.

9. H. Lei, Y. Liu, Y. Zhang, and Y. Hu, "Ground Deformation Behaviour Induced by Overlapped Shield Tunnelling Considering Vibration Loads of Subway Train in Sand," *Acta Geotechnica* 18, no. 1 (2023): 519–533.

10. Z. Ding, X. Huang, M.-M. Sun, L.-Y. Xu, Z.-G. Huang, and Q.-H. Zhou, "Experimental Study on the Influence of Cracks on Tunnel Vibration Under Subway Train Load," *Tunnelling and Underground Space Technology* 142 (2023): 105444.

11. W. Luo and S. Deng, "Numerical and In-Situ Investigation on Bilateral Double-Wall Barriers in Mitigating Metro Train-Induced Vibrations," *Construction and Building Materials* 469, no. 28 (2025): 140502.

12. Y. Qiu, C. Zou, J. Wu, Z. Shen, and Z. Zhong, "Building Vibration Measurements Induced by Train Operation on Concrete Floor," *Construction and Building Materials* 394, no. 29 (2023): 132283.

13. J. Yang, S. Zhu, W. Zhai, et al., "Prediction and Mitigation of Train-Induced Vibrations of Large-Scale Building Constructed on Subway Tunnel," *Science of the Total Environment* 668, no. 10 (2019): 485–499.

14. K. Zhong, X. Li, and Z. Zhou, "High-Speed Train-Induced Vibration of Bridge-Soft Soil Systems: Observation and MTF-Based ANSYS Simulation," *Buildings* 14, no. 8 (2024): 2575.

15. A. Oral, O. Subasi, Cın Korkmaz, and I. Lazoglu, "A Novel Transient Vibration and Noise Reducer (TVR) for Vibratory Machines," *Applied Acoustics* 201 (2022): 109139.

16. P. Xie, L. Zhang, M. Li, S. F. S. Lau, and J. Huang, "Elevator Vibration Signal Denoising by Deep Residual U-Net," *Measurement* 225, no. 15 (2024): 113976.

17. X. Bao and C. Shi, "Ambient Vibration Responses Denoising for Operational Modal Analysis of a Jacket-Type Offshore Platform," *Ocean Engineering* 172, no. 15 (2019): 9–21.

18. K. Tao, M. Xu, and Q. Wang, "ASSA-VMD-SI and Frechet Method of Pipe Vibration for Noise Reduction and Leakage Identification," *Measurement* 242 (2025): 116277.

19. M. Dalmasso, M. Civera, V. De Biagi, C. Surace, and B. Chiaia, "Conditional Generative Adversarial Networks for the Data Generation and Seismic Analysis of Above and Underground Infrastructures," *Tunnelling and Underground Space Technology* 157 (2025): 106285.

20. M. Dalmasso, M. Civera, and B. Chiaia, "The Seismic Response and Resilience of Nearby Underground Infrastructures," *Bridge Maintenance, Safety, Management, Digitalization and Sustainability* 1, no. 8 (2025): 183.

21. G. Qi, Z. Zhao, R. Zhang, et al., "Optimized VMD Algorithm for Signal Noise Reduction Based on TDLAS," *Journal of Quantitative Spectroscopy and Radiative Transfer* 312 (2024): 108807.

22. Y. Zheng, B. Liao, F. Shen, et al., "Study on the Influence of Train Dynamic Load on Underneath Tunnel Cast-In-Situ Concrete in Early Age," *Shock and Vibration* 2022 (2022): 2464675.

23. M. Mahmoudi and A. M. Rajabi, "A Numerical Simulation Using FLAC3D to Analyze the Impact of Concealed Karstic Caves on the Behavior of Adjacent Tunnels," *Natural Hazards* 117, no. 1 (2023): 555–577.

24. Z. Gu, H. Wei, Z. Liu, and M. Zhang, "Dynamic Response Mechanism of Silt Ground Under Vibration Load," *Sustainability* 14, no. 16 (2022): 10335.

25. Y. Xiao, M. He, Y. Qiao, W. Cai, Y. Jiang, and H. Zhu, "A Novel Implementation Method of GZZ-Based Constitutive Model Into FLAC3D," *Tunnelling and Underground Space Technology* 145 (2024): 105601.

26. J. Wang and L. Dong, "Research and Application of Mine Microseismic Signal Processing Based on Joint PKO-VMD With Wavelet Threshold Functions," *Measurement* 256, no. 1 (2025): 118159.

27. B. Jia, S. Li, D. Liu, and S. Wu, "Application of Low-Frequency Processing Method Based on VMD Algorithm in Blasting Signal Processing," *Shock and Vibration* 2022 (2022): 5779714.

28. Q. Wang, P. Geng, J. Chen, and C. He, "Dynamic Ddiscrimination Method of Seismic Damage in Tunnel Portal Based on Improved Wavelet Packet Transform Coupled With Hilbert-Huang Transform," *Mechanical Systems and Signal Processing* 188 (2023): 110023.